Title

Experimental validation of the influence of white matter anisotropy on the intracranial EEG forward solution

Journal

Journal of Computational Neuroscience, 29(3)

ISSN

1573-6873

Authors

Bangera, Nitin B.
Schomer, Donald L.
Dehghani, Nima
et al.

Publication Date

2010-12-01

DOI

10.1007/s10827-009-0205-z

Peer reviewed

J Comput Neurosci (2010) 29:371–387
DOI 10.1007/s10827-009-0205-z

Experimental validation of the influence of white matter anisotropy on the intracranial EEG forward solution

Nitin B. Bangera · Donald L. Schomer · Nima Dehghani · Istvan Ulbert · Sydney Cash · Steve Papavasiliou · Solomon R. Eisenberg · Anders M. Dale · Eric Halgren

Received: 31 July 2009 / Revised: 5 December 2009 / Accepted: 11 December 2009 / Published online: 9 January 2010

Abstract Forward solutions with different levels of complexity are employed for localization of current generators, which are responsible for the electric and magnetic fields measured from the human brain. The influence of brain anisotropy on the forward solution is poorly understood. The goal of this study is to validate an anisotropic model for the intracranial electric forward solution by comparing with the directly measured 'gold standard'. Dipolar sources are created at known locations in the brain and intracranial electroencephalogram (EEG) is recorded simultaneously. Isotropic models with increasing level of complexity are generated along with anisotropic models based on Diffusion tensor imaging (DTI). A Finite Element Method based forward solution is calculated and validated using the measured data. Major findings are (1) An anisotropic model with a linear scaling between the eigenvalues of the electrical conductivity tensor and water self-diffusion tensor in brain tissue is validated. The greatest improvement was obtained when the stimulation site is close to a region of high anisotropy. The model with a global anisotropic ratio of 10:1 between the eigenvalues (parallel: tangential to the fiber direction) has the worst performance of all the anisotropic models. (2) Inclusion of cerebrospinal fluid as well as brain anisotropy in the forward model is necessary for an accurate description of the electric field inside the skull. The results indicate that an anisotropic model based on the DTI can be constructed non-invasively and shows an improved performance when compared to the isotropic models for the calculation of the intracranial EEG forward solution.

Keywords Forward solution · White matter anisotropy · Intracranial EEG · Validation · FEM · Finite element model · Source localization

Action Editor: Abraham Zvi Snyder

Electronic supplementary material The online version of this article (doi:10.1007/s10827-009-0205-z) contains supplementary material, which is available to authorized users.

N. B. Bangera · S. R. Eisenberg
Department of Biomedical Engineering, Boston University, Boston, MA, USA

N. B. Bangera · N. Dehghani · A. M. Dale · E. Halgren
Multimodal Imaging Laboratory,
Departments of Radiology and Neurosciences,
University of California at San Diego,
La Jolla, CA, USA

D. L. Schomer · S. Papavasiliou
Department of Neurology, Beth Israel Deaconess Medical Center, Boston, MA, USA

I. Ulbert
Institute for Psychology of the Hungarian Academy of Sciences, Budapest, Hungary

S. Cash
Department of Neurology, Massachusetts General Hospital, Boston, MA, USA

N. B. Bangera (✉)
Alexian Brothers Center for Brain Research—Illinois MEG Center,
955 Beisner Rd, Niehoff Pavilion,
Elk Grove Village, IL 60007, USA
e-mail: nitinb@bu.edu

1 Introduction

The simulation and calculation of the electromagnetic fields for a given head geometry and source distribution inside the brain is known as the forward problem or the forward solution. Localization of brain sources from measured bioelectromagnetic fields is carried out using an inverse

procedure, which incorporates a forward solution, and is dependent on its accuracy. The primary question in volume conductor modeling is how accurate a description of the geometry and conductivities of the tissues inside the head is necessary for accurate forward solutions and as a result for accurate source localizations. In this paper, we address this issue primarily for the intracranial domain by comparing the intracranial forward solutions of progressively detailed realistic models to experimental data obtained with known source locations.

Experimental studies have been carried out in 'tank' models of the head and *in vivo*. A tank model study (Henderson et al. 1975), using a skull filled with saline and an artificial "scalp," obtained localization accuracy of about 1 cm. A human skull phantom implanted with multiple dipoles was utilized to examine the effects of forward methods on EEG and Magnetoencephalography (MEG) localization accuracy by using a locally fitted sphere model and Boundary Element model (BEM) (Leahy et al. 1998). Spherical model was found to generate slightly greater error than the BEM except for locations such as the frontal dipolar region where the localization error was about 1 cm greater than the BEM due to poor spherical fits in the region. Smith et al. (Smith et al. 1983) passed a rectangular pulse through depth electrodes *in vivo*, and compared the measured intracerebral potentials to analytically calculated values using different values for conductivities. Results were found to be consistent with homogeneous medium. However, a detailed quantification of the differences between measured and calculated values was not carried out for this study, and an inhomogeneous model was not tested. Further analysis of these data using inverse solutions gave a localization accuracy of about 2 cm when performed using a spherical forward solution (Smith et al. 1985). Localization accuracy ranging from 0.5 to 2 cm was obtained for artificial sources from subdural electrodes placed on the surface of the brain (Salu 1990). A homogeneous spherical model with no correction for the skull defect was used for the forward solution. A direct comparison between MEG and EEG localization accuracy using implanted sources *in vivo* found an average error of 0.8 cm for MEG and 1 cm for EEG using a multi-layered spherical forward model (Cohen et al. 1990). An average localization of about 1 cm was also obtained from scalp potentials recorded during depth stimulation irrespective of whether the forward model was a multi-layered spherical model (Cuffin et al. 1991) or the more realistic boundary element model (Cuffin et al. 2001). Surprisingly, the spherical model produced nearly the same localization accuracy as the realistic shaped brain model suggesting that several other modeling errors other than the non-spherical shape of the head could be involved. Possible modeling errors could be inaccurate tissue conductivity values, tissue anisotropy, variations in tissue thickness and conductivity inside the head. In all of the previous experimental studies, a spherical or BEM model has been used and the measurements have been extracranial with the sole exception of (Smith et al. 1985). This study did record intracranial potentials *in vivo* but with a spherical forward solution which did not model the actual shape of the head and its compartments, nor the inhomogeneity, and anisotropy known to occur within the head volume. There has been no study to quantify the accuracy of a realistic anisotropic forward solution with actual experimental data, in particular with intracranial measurements. Some recent studies have shown the clinical utility of advanced source imaging techniques in localizing epileptogenic loci using BEM (Cuffin 1998) and finite element models (FEM) (Plummer et al. 2007). However these methods are not yet routinely used in clinical settings due to their high computational cost and the lack of direct validation of these techniques with experimental data.

In this paper, patient-specific FEM-based head models generated using multimodal images are utilized for validating a realistic head model for the intracranial forward solution using intracranial electric field measurements from the human brain. Isotropic models with increasing level of detail as well as multiple anisotropic models to incorporate white matter conductivity information non-invasively are tested for accuracy by directly comparing model results with the intracranial potentials obtained from *in vivo* depth stimulation in human subjects. We know that the electric field measured on the scalp is likely to be influenced by anisotropy in both the skull and the brain, whereas the electric field inside the cranial cavity is likely to be influenced only by anisotropy of the white matter. Thus, the use of intracranial rather than scalp measurements helps to segregate the effects of the two sources of anisotropy in human head (the white matter and the skull) and investigate the influence of brain anisotropy more closely.

Also, with the aid of novel visualizations we present some unique insights into the influence of the underlying tissue conductive properties on the bioelectric field qualitatively. Reductions in forward model errors using FEM could lead to improved source localizations of seizures with the eventual goal of surgery without the need of invasive EEG monitoring. In addition to its application in source localization, this could provide vital insights when utilized to study deep brain stimulation (DBS), which is commonly used for treatment of Parkinson's disease, as well as brain mapping to define eloquent tissue prior to surgical resections. DBS is also being actively evaluated for application to other diseases including stroke, coma, addiction, pain, depression, and epilepsy. The underlying hypothesis in our models is that details do matter, and with the aid of experiments in human subjects, we investigate the degree

of anatomical detail necessary in the forward model for EEG to improve the predictive value of the model.

2 Materials and methods

2.1 Experimental methods: human subjects, dipole generation set-up and intracranial EEG measurement set-up

The 4 subjects (BI14, BI15, BI17 and BI18) were patients with medically intractable epilepsy who underwent monitoring with intracranial depth electrodes for a period of 2–4 weeks prior to surgery at the Beth Israel Deaconess Medical Hospital (Boston, MA). Informed consent was obtained from the subjects (four females aged between 24 and 50 yrs) and the experimental protocol was approved by the subcommittee on human studies at the Beth Israel Deaconess Medical Hospital (BIDMC). The implanted electrodes were cylindrical platinum-iridium contacts mounted on hollow plastic catheters with wires connecting to each contact. The contacts were 1 mm in diameter and 2 mm in length and were spaced 5 mm apart on each catheter. Each subject had 5 catheters on each side of the head with 7 contacts on each catheter. The catheters passed through the skull through electrically non-conducting plastic plugs which completely filled the 3 mm diameter holes used to insert the catheters into the brain. The dipolar source was created in the brain by passing a biphasic square current pulse through alternating contacts on the implanted catheter (See Appendix A for additional details on the biphasic pulse generation). 3-D representation of implanted electrodes locations are shown in Fig. 1(b) and (c).

The schematic of the experimental set-up is given in Fig. 1(a). Each artificial dipole (stimulation) is referred to by the electrode name followed by the contact numbers (1–7 where 1 refers to the deepest contact) for the monopolar source and monopolar sink (e.g. LA12). For subjects BI14, BI15 and BI17 the current waveform had a total duration of 42.5 ms and amplitude of $8\,\mu A$. For subject BI18, the waveform had a total duration of 37.5 ms and the current amplitude was increased to $100\,\mu A$ (to increase signal-to-noise ratio). The charge density (charge/cm^2/ph) used in this study (maximum of ~ $25\mu C/cm^2/ph$ at ~1.7 $\mu C/ph$) was below the critical level of 40 $\mu C/cm^2/ph$ for neural damage (Mccreery et al. 1990; Merill Merill et al. 2005). The current levels were well below the stimulation levels used in later clinical stimulation sessions to elicit a discharge (Tehovnik 1996) and too low to produce any sensations.

The intracranial potential was obtained while passing a biphasic square wave current pulse using a recording system developed by Ulbert et al. (Ulbert et al. 2001). The intracranial potential was recorded using a high-impedance preamplifier and band-filtered by the main amplifier (0.1–500 Hz) with 16-bit resolution and a digitization rate of 2000 Hz. The intracranial measurements were done in a bipolar fashion (between alternate contacts) and then converted to a referential montage offline. A sample stimulation pulse and intracranial potential waveform recorded during dipole stimulation from subject BI18 is shown in Fig. 1(d) and (e) respectively. 3-D locations of the intracranial electrode contacts are obtained accurately by aligning the post-implantation CT images with the MRI images.

A summary of total number of stimulation sites, recording electrodes and average SNR across all stimulation sites for the 4 subjects is given in Table 1. Measurements with an SNR>5 are used for comparisons with the model predicted values (See Appendix A for the method used for calculating the SNR). For subject BI18, all recording electrodes had the required SNR due to the higher current amplitude whereas for subjects BI14, BI15 and BI17 electrodes from same side of the brain as the stimulation site had the requisite SNR.

2.2 FEM model types

A detailed description of the development of a FEM model from multimodal imaging methods (Computed Tomography [CT], T1-MRI, Proton Density [PD]-MRI and Diffusion Tensor Imaging, DTI) is described elsewhere (Bangera et al., manuscript in submission). The resultant FEM model for BI18 has 256772 nodes and 1488774 linear (first order) tetrahedral elements (243711 nodes and 1415024 elements for BI17; 272380 nodes and 1569546 elements for BI15; 273230 nodes and 1574629 elements for BI14). The isotropic and anisotropic models generated for each subject are listed below.

2.2.1 Isotropic models

- Model **ISO_I** has 3 tissue types (1 intracranial tissue type): Brain, Skull and Scalp.
- Model **ISO_II** has 4 tissue types (2 intracranial tissue types): Brain, CSF, Skull and Scalp.
- Model **ISO_III** has all 15 unique tissue types (6 intracranial tissue types) as listed in Table 2.

2.2.2 Anisotropic models

Specification of the anisotropy in each voxel was based on each individual patient's DTI. Following the proposition by Basser et al., we assumed that the conductivity tensor and diffusion tensor share common eigenvectors, i.e. $V_\sigma = V_d$ (Basser et al. 1994). The eigenvalues for conductivity tensor are different from the diffusion tensor eigenvalues and are simulated to create multiple anisotropic models as shown below. The eigenvalues along the transverse direc-

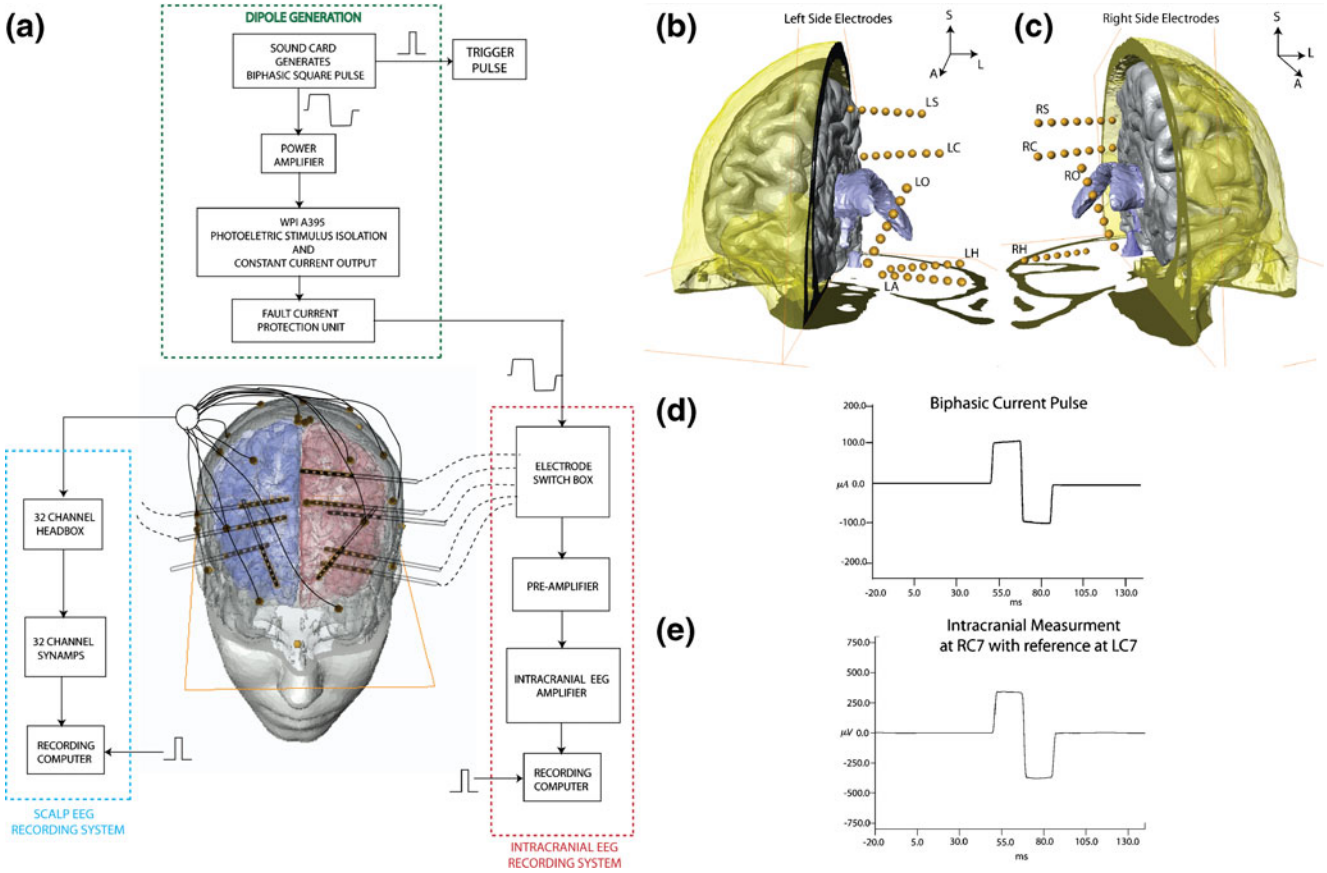

Fig. 1 *Experimental set-up*. (**a**) Overall schematic shows the dipole generation set-up and the intracranial potential recording set-up. (**b**) Anterior view showing left side electrodes in subject BI18 with respect to the ventricles (colored in blue), right cortex (in gray) and cross-section of skull (O: Orbito-frontal, C: Cingulate, S: Supplementary Motor, A: Amygdala, H: Hippocampus). (**C**) Anterior view of right side electrodes. (**d**) Sample injected current pulse shows $100\,\mu A$ biphasic current pulse with a upslope setting of 25 to compensate for "droop" **(e)** shows a sample waveform measured from contact number 7 on intracranial depth electrode RC (Right Cingulate)

tion (perpendicular to the fiber direction) are denoted as σ_λ^{trans1} and σ_λ^{trans2}. σ_λ^{long} is the eigenvalue along the fiber direction (also called the longitudinal direction) such that $\sigma_\lambda^{\text{long}} > \sigma_\lambda^{\text{trans1}} \geq \sigma_\lambda^{\text{trans2}}$.

- ANISO_WM_I

The linear anisotropic white matter model ANISO_WM_I is based on an empirical study relating the conductivity and diffusion tensors (Tuch et al. 2001). In this model a linear relationship between the conductivity tensor eigenvalues (σ_λ) and diffusion tensor eigenvalues (d_λ) is assumed for white matter.

$$\sigma_\lambda = kd_\lambda \;\forall \lambda = 1,2,3 \tag{1}$$

The scaling factor 'k' is determined by optimizing the error cost function as function of *'k'* using intracranial measurements during dipole stimulations (see method for

Table 1 Summary of total number of stimulation sites, recording electrodes and average SNR across all stimulation sites for all subjects in this study (LA: Left Amygdala, LH: Left Hippocampus, LS: Left Supplementary Motor, LC: Left Cingulate, LO: Left Orbito-frontal, RA: Right Amygdala, RH: Right Hippocampus, RO: Right Orbito-frontal, RS: Right Supplementary Motor, RC: Right Cingulate)

Subject	Number of dipole sites	Recording electrodes	Average SNR across all stimulation sites
BI14	6	RO,RS,RC,LC,LO	34
BI15	16	RO,RS,RC,RA,RH,LO,LA,LS,LC,LH	22
BI17	16	RO,RH,RC,LC,LO	50
BI18	23	RO,RS,RC,RH,LO,LA,LS,LC,LH	124

Table 2 Optimized Tissue Conductivities for isotropic model types ISO_I, ISO_II and ISO_III

Tissue name	Model type ISO_I:3 tissue			Model type ISO_II:4 tissue			Model type ISO_III: all tissue		
	Material assigned	Starting value S/m	Optimized value S/m	Material assigned	Starting value S/m	Optimized value S/m	Material assigned	Starting value S/m	Optimized value S/m
Gray Matter (GM)	Brain	0.33	0.3373622	Brain	0.33	0.19129234	GM	0.3521	0.297268568
White Matter (WM)	Brain	0.33	0.3373622	Brain	0.33	0.19129234	WM	0.1466	0.154717786
Cerebrospinal Fluid (CSF)	Brain	0.33	0.3373622	CSF	1.79	1.58388257	CSF	1.79	1.584524266
Ventricles	Brain	0.33	0.3373622	Brain	0.33	0.19129234	CSF	1.79	1.584524266
Cerebellum GM	Brain	0.33	0.3373622	Brain	0.33	0.19129234	Cerebellum	0.154	0.154
Cerebellum WM	Brain	0.33	0.3373622	Brain	0.33	0.19129234	Cerebellum	0.154	0.154
Sub-Cortical	Brain	0.33	0.3373622	Brain	0.33	0.19129234	Brain_general	0.25	0.225913002
Skull	Skull	0.015	0.0059406	Skull	0.015	0.00661725	Skull	0.015	0.004119296
Soft bone	Skull	0.015	0.0059406	Skull	0.015	0.00661725	Soft_bone	0.04	0.009467393
Sinus	Skull	0.015	0.0059406	Skull	0.015	0.00661725	Air	1.00E-17	1.00E-17
Air pockets	Skull	0.015	0.0059406	Skull	0.015	0.00661725	Air	1.00E-17	1.00E-17
Optic chiasm	Skull	0.015	0.0059406	Skull	0.015	0.00661725	Brain_general	0.25	0.225913002
Muscle	Scalp	0.44	0.5065091	Scalp	0.44	0.50357474	Muscle	0.1	0.200025083
Fat	Scalp	0.44	0.5065091	Scalp	0.44	0.50357474	Fat	0.0367	2.76756041
Eyes	Scalp	0.44	0.5065091	Scalp	0.44	0.50357474	Eyes	1.55	6.519239245
Spinal cord	Scalp	0.44	0.5065091	Scalp	0.44	0.50357474	Spinal_cord	0.5714	0.5714
Teeth	Scalp	0.44	0.5065091	Scalp	0.44	0.50357474	Teeth	0.020028	0.020028
Blood	Scalp	0.44	0.5065091	Scalp	0.44	0.50357474	Blood	0.6667	0.6667
Scalp	Scalp	0.44	0.5065091	Scalp	0.44	0.50357474	Scalp	0.44	0.518011512
Sagittal Sinus	Brain	0.44	0.3373622	Brain	0.33	0.19129234	Blood	0.6667	0.6667

optimization below). Remaining tissue types are identical to ISO_III.

- ANISO_WM_II

The second anisotropic model is based on the reported conductivity measurements of white matter anisotropy (Nicholson 1965) of 10:1 (parallel to perpendicular to fiber direction). For white matter elements, the conductivity eigenvalues for directions perpendicular to the fiber direction are assigned equal values:

$$\sigma_{\lambda}^{trans1} = \sigma_{\lambda}^{trans2} = \sigma_{\lambda}^{trans} \tag{2}$$

and a scaling between the eigenvalues along the fiber direction to eigenvalues in transverse direction is given by the scaling factor k:

$$\sigma_{\lambda}^{long} = k\sigma_{\lambda}^{trans} \tag{3}$$

Due to a lack of conclusive measurement of the anisotropic ratio, ANISO_WM_II was generated with different scaling values (k=2, 5, 7, 10) and are listed as model types ANISO_WM_II_a, ANISO_WM_II_b, ANISO_WM_II_c and ANISO_WM_II_d respectively. For an applied ratio $\sigma_{\lambda}^{long} : \sigma_{\lambda}^{trans}$, the eigenvalues are constrained using a *'Volume constraint'* put forth by Wolters et al. (Wolters 2003) , which retains the geometric mean of the eigenvalues and the volume of the conductivity tensor between the isotropic and anisotropic case.

- ANISO_IC

This model is an extension of model ANISO_WM_I. In addition to anisotropy in the white matter, this model also assumes a linear scaling between conductivity tensor eigenvalues σ_{λ} and diffusion tensor eigenvalues d_{λ} for mesh elements labeled as gray matter and subcortical.

2.3 Optimization of electrical conductivity of head tissue

There is a large variability in reported values for tissue conductivities with a dependence on frequency and temperature of measurement for tissues such as gray matter, white matter and the skull (Akhtari et al. 2002; Baumann

Baumann et al. 1997; Burger and Van Milaan 1943; Gabriel et al. 1996; Geddes and Baker 1967; Latikka et al. 2001; Law 1993; Lindenblatt and Silny 2001; Okada et al. 1994; Oostendorp et al. 2000; Ranck and Be Meritt 1965). To overcome the problem associated with the uncertainties in measured values, a multi-dimensional optimization strategy is employed to find a 'best-fit' conductivity value (See Appendix B for the formulation of the optimization problem). Optimized conductivities for isotropic models are listed in Table 2. For anisotropic models ANISO_WM_I and ANISO_IC, an optimized scaling k=0.5708 between conductivity tensor eigenvalues σ_λ and diffusion tensor eigenvalues d_λ of white matter is empirically obtained. For the four sub-types of model ANISO_WM_II, the white matter conductivities (eigenvalues) are listed in Table 3. The isotropic tissues in the anisotropic models are assigned isotropic conductivities identical to model ISO_III.

2.4 Error criteria for forward solution accuracy

The Relative Difference Measure (RDM) is used to quantify the comparisons made between the model predicted field values and experimental data. If V_{calc} and V_{meas} are the calculated and measured vectors of length M (M is the number of sensors) respectively then:

$$RDM(V_{calc}, V_{meas})\% = \sqrt{\sum_{i=1}^{M}\left(\frac{V^i_{calc}}{\sqrt{\sum_{i=1}^{M}\left(V^i_{calc}\right)^2}} - \frac{V^i_{meas}}{\sqrt{\sum_{i=1}^{M}\left(V^i_{meas}\right)^2}}\right)^2} \times 100 \quad (4)$$

RDM is a measure of topography error introduced by Meijs et al. (Meijs et al. 1989). Minimum error corresponds to a RDM of zero. RDM is unaffected by scaling in amplitude between two datasets being compared which makes it a better choice as compared to the Goodness of Fit (GF) measure to compare topographical differences between two EEG datasets. The goodness of fit (GF) is defined in Eq. (B.2) (See Appendix B).

2.5 Visualization techniques for volume currents

The volume currents (electric current density vector fields) are visualized as a texture in 2-D and as illuminated stream Tubes in 3-D by using the 'PlanarLIC' and 'DisplayISL' modules respectively in AMIRA (Visage Imaging 2007). The 'PlanarLIC' module intersects an arbitrary 3D vector field and visualizes its directional structure in the cutting plane using a technique called line integral convolution (LIC). The LIC algorithm works by convolving a random noise image along the projected field lines of the incoming vector field using a piecewise-linear hat filter (Visage Imaging 2007). The synthesized texture clearly reveals the directional structure of the vector field inside the cutting plane. The 'DisplayISL' visualizes a 3D vector field using so-called illuminated field lines (Malte Zöckler and Hans-Christian 1996). The module computes a large number of field lines by integrating the vector field starting from random seed points. The lines are displayed using a special illumination technique, which gives a much better spatial understanding of the field structure than ordinary constant-colored lines (Visage Imaging 2007).

3 Results

It should be noted that subject BI18 injected with a current dipole with moment 500 nA-m provided the best data-set as the higher current amplitude made it possible to obtain measurements with high SNR from recording electrodes on both sides of the head (60 sensor locations for each of the 23 stimulation sites). For subjects BI17, BI15 and BI14 some of the measurement electrodes were excluded from analysis as the minimum SNR requirement (SNR>5) was not met due to a smaller current injection (dipole moment 40 nA-m). The recording electrodes used for each stimulation site in subjects BI17, BI15 and BI14 are listed in Supplementary Fig. 2.

3.1 Validation with experimental data

The intracranial forward solution obtained using the isotropic and anisotropic models were compared to the

Table 3 Simulated values of White Matter Eigenvalues in S/m along the longitudinal (along fiber direction) and transverse directions (perpendicular to fiber directions) for a given anisotropic ratio

Volume constraint: White matter (S/m)				
Model type	$\sigma_\lambda^{long} : \sigma_\lambda^{trans}$	σ_{ISO_WM}	σ_λ^{long}	σ_λ^{trans}
ANISO_WM_II_a	2:1	0.1547	0.2456	0.1228
ANISO_WM_II_b	5:1	0.1547	0.4524	0.0905
ANISO_WM_II_c	7:1	0.1547	0.5662	0.0809
ANISO_WM_II_d	10:1	0.1547	0.7181	0.0718

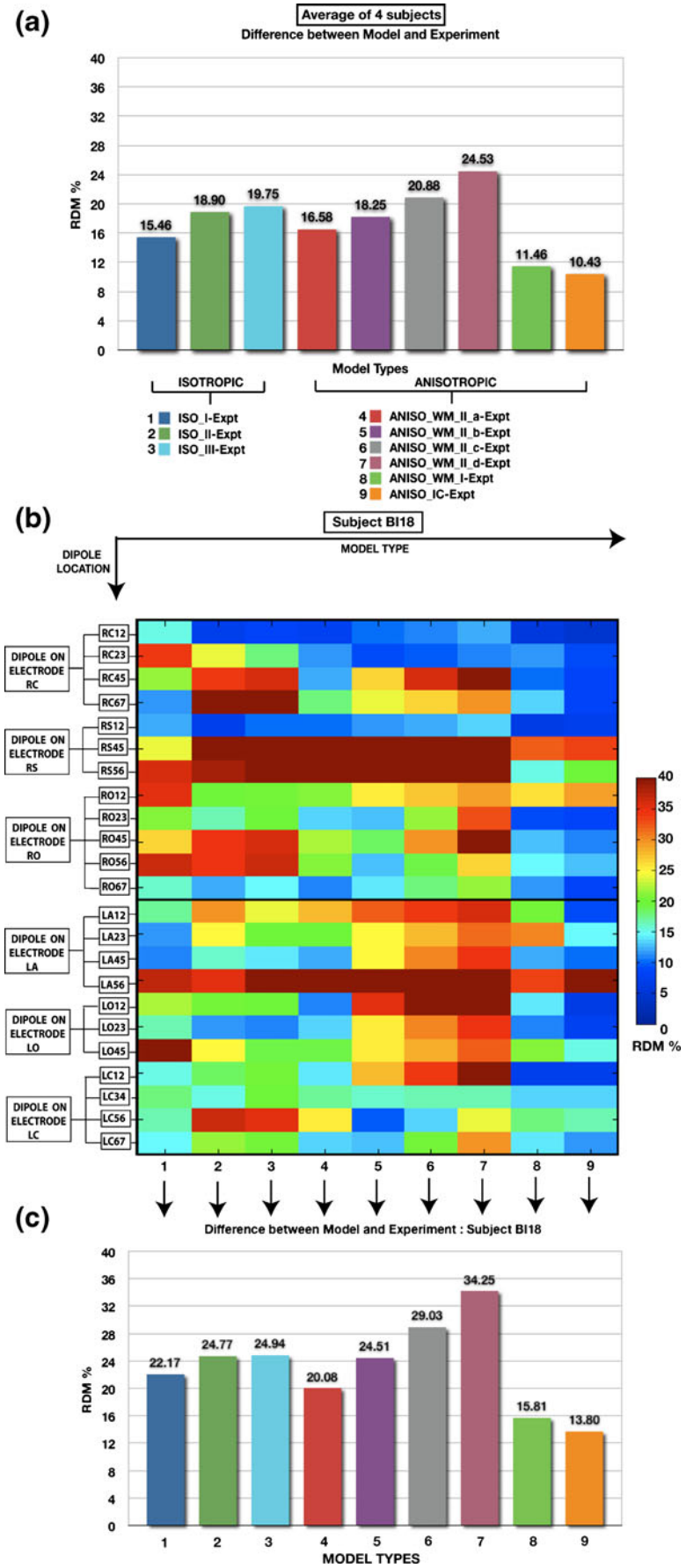

Fig. 2 *Accuracy of different models compared to actual measurements.* Accuracy is quantified as the Relative Difference Measure (RDM); Lower values indicate greater model accuracy. (**a**) Plot of RDM between intracranial potentials predicted by a head model and measured potentials averaged across 61 stimulation sites in 4 subjects. Isotropic FEM models differ in their numbers of tissue types (3, 4 and 15 for models ISO_I, II and III; in columns 1-3 from left). In some anisotropic models the anisotropy is assumed to be uniform (middle); these differ in the conductance increase parallel to the fiber direction (parallel/transverse ratios of 2, 5, 7, and 10 for models ANISO_WM_II_a, b, c, and d; in columns 4-7). In other anisotropic models, the degree of anisotropy is estimated from DTI data, and applied to the white matter only (ANISO_WM_I; column 8), or to both white and gray matter (ANISO_IC; column 9). Model types are color-coded as indicated below the bar-chart. (**b**) Error (color-coded RDM) for 7 different model types (columns) and 23 different stimulation sites (rows) in BI18 (averaged across all recording electrodes). Stimulation site is given as the electrode name followed by the contact numbers for monopolar source and sink. (**C**) RDM between model and experiment when averaged over the 23 stimulation sites in BI18. In both group and individual subject experiments, the highest accuracy was obtained with the ANISO_IC model, which estimated anisotropy for both gray and white matter from individual subject DTI. Individual data for subjects BI14, BI15 and BI17 are shown in Supplementary Figure 1

experimental data obtained from stimulation of an artificial dipole. Figure 2(a) plots the RDM between the model-predicted potentials and those actually measured, as averaged across 4 subjects. Figure 2(b) plots the RDM between the potentials calculated using each of the nine models, and the experimental data collected from subject BI18 for each stimulation site in the brain over all sensor locations (See Fig. 1(A, C, E) in the supplementary section for the same measures plotted in subjects BI17, BI15 and BI14, respectively). Figure 2(c) plots the RDM averaged across all stimulation sites for the different models for BI18 (See Fig. 1(B, D, F) in the supplementary section for the same measures plotted in subjects BI17, BI15 and BI14, respectively). For a closer inspection of the errors between the model and the experimental data, we also plot the RDM's for individual electrode and for each stimulation site in BI18 in Fig. 3 (See Fig. 2 in supplementary section for RDM's at individual electrodes in subjects BI17, BI15 and BI14).

3.2 Comparison between isotropic models

RDM between the model and experimental data was ~25% for isotropic models ISO_II and ISO_III in BI18 (See Fig. 2 (c)). Contrary to expectations, results from Fig. 2(c) show that the 3-tissue isotropic model (ISO_I) on an average performs slightly better (error reduced by ~3%) than the 4-tissue model (ISO_II) and the 15 tissue isotropic model (ISO_III). The results were similar in BI17, BI15 and BI14 where ISO_I performed better than other two isotropic models (ISO_II and ISO_III). However this represented the overall errors and did not show the improvements provided by the model ISO_II and ISO_III at specific sites due to inclusion of ventricles and CSF. The presence of stimulation and measurement electrodes on opposite sides of the hemisphere in subject BI18 made it possible to obtain some quantitative evidence of the benefits of inclusion of CSF in the model. We study the case of stimulation at a site RS12 which is close to the inter-hemispherical space (filled with CSF) in subject BI18 and measurement at electrode LS lying in the opposite hemisphere of the brain. Electrode LS has contacts close to CSF (See Fig. 4(a)) which makes it a good candidate to study the effects of CSF. Figure 4(c) and (d) provide visualizations of the volume currents generated in a 3-tissue isotropic model and 15-tissue isotropic model respectively on an axial plane containing the electrode LS. The impact of CSF between the hemispheres can be seen from the pattern of increased current densities in the areas surrounding electrode LS. RDM at electrode LS due to stimulation at RS12 reduced from 21% for ISO_I to ~7% and 8% for both ISO_II and ISO_III respectively (See Fig. 3(f)). For the same case the RDM at electrode LS was 7% in model ANISO_WM_I, which suggests that the improvement could be as a result of the inclusion on anisotropy. To differentiate between the effects of CSF and anisotropy, we generated a modified version of ANISO_WM_I where the CSF was removed and substituted as GM. RDM for the modified version of ANISO_WM_I (without CSF) now increased to 16%; thereby suggesting that the improvements are primarily due to the addition of CSF. Similar improvements were obtained for stimulations at sites RC12 and LC12 for measurements at electrodes in the opposite hemisphere at LS and RS respectively. For stimulation at RC12 (also near the inter-hemispherical CSF) the RDM at LS dropped from a large 62% error generated by ISO_I to ~ 17% generated by ISO_III (See Fig. 3(d)). For the case of stimulation site LC12, RDM at electrode RS dropped from 16% for ISO_I to 8% for ISO_III (See Fig. 3 (a)). These findings highlight the value of including a CSF compartment in the head model.

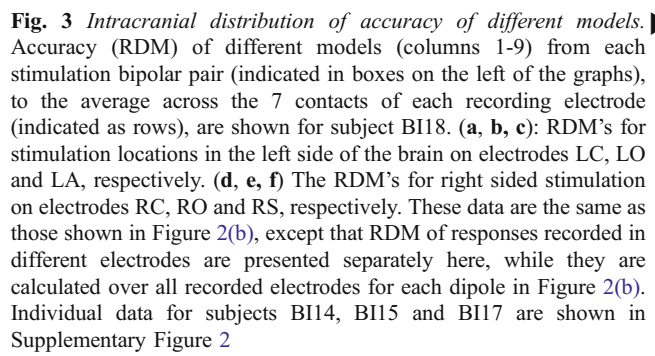

Fig. 3 *Intracranial distribution of accuracy of different models.* Accuracy (RDM) of different models (columns 1-9) from each stimulation bipolar pair (indicated in boxes on the left of the graphs), to the average across the 7 contacts of each recording electrode (indicated as rows), are shown for subject BI18. (**a**, **b, c**): RDM's for stimulation locations in the left side of the brain on electrodes LC, LO and LA, respectively. (**d**, **e, f**) The RDM's for right sided stimulation on electrodes RC, RO and RS, respectively. These data are the same as those shown in Figure 2(b), except that RDM of responses recorded in different electrodes are presented separately here, while they are calculated over all recorded electrodes for each dipole in Figure 2(b). Individual data for subjects BI14, BI15 and BI17 are shown in Supplementary Figure 2

3.3 Isotropy vs. Anisotropy

Results from Fig. 2 show that the linear anisotropic model ANISO_IC generates the least errors of all the models when the RDM was averaged across all subjects. The biggest impact of ANISO_IC is seen in subject BI18 (Compare Fig. 2(c) with Supplementary Fig. 1(A, D and F)). This can be attributed to the inter-subject variability in electrode locations as well as larger number of stimulation sites and measurement electrodes with high SNR (due to higher current) in BI18 as compared to the other three subjects (BI17, BI15 and BI14). RDM for individual stimulation sites in Fig. 2(b) show that ANISO_IC gives smaller errors when compared to ISO_III for all stimulation sites in BI18. Similarly when compared to model ISO_I, ANISO_IC shows improved performance for all 23 stimulation sites in BI18 except at RS45 (see Fig. 2(b)). The difference between the average RDM's generated by different groups in BI18 was found to be statistically significant ($P<0.01$). Pairwise comparisons between model types in BI18 also found ANISO_IC to perform significantly better than other models ($P<0.01$). To understand the reductions in RDM's between the model and experimental data due to anisotropy,

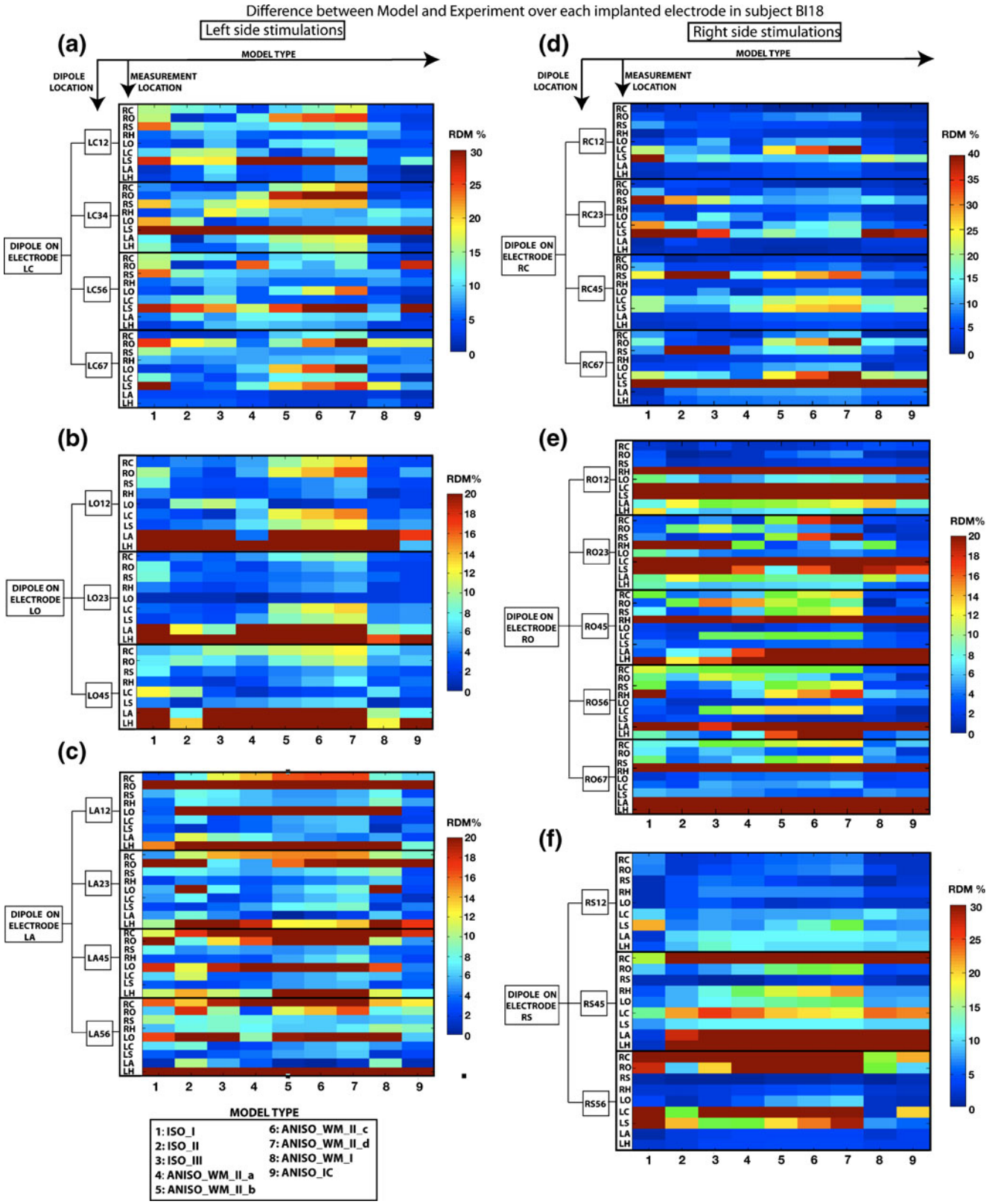
Difference between Model and Experiment over each implanted electrode in subject BI18
Left side stimulations
Right side stimulations
(a)
(b)
(c)
(d)
(e)
(f)
MODEL TYPE
DIPOLE LOCATION
MEASUREMENT LOCATION
DIPOLE ON ELECTRODE LC
DIPOLE ON ELECTRODE LO
DIPOLE ON ELECTRODE LA
DIPOLE ON ELECTRODE RC
DIPOLE ON ELECTRODE RO
DIPOLE ON ELECTRODE RS
LC12
LC34
LC56
LC67
LO12
LO23
LO45
LA12
LA23
LA45
LA56
RC12
RC23
RC45
RC67
RO12
RO23
RO45
RO56
RO67
RS12
RS45
RS56
RDM %
RDM%
MODEL TYPE
1: ISO_I
2: ISO_II
3: ISO_III
4: ANISO_WM_II_a
5: ANISO_WM_II_b
6: ANISO_WM_II_c
7: ANISO_WM_II_d
8: ANISO_WM_I
9: ANISO_IC

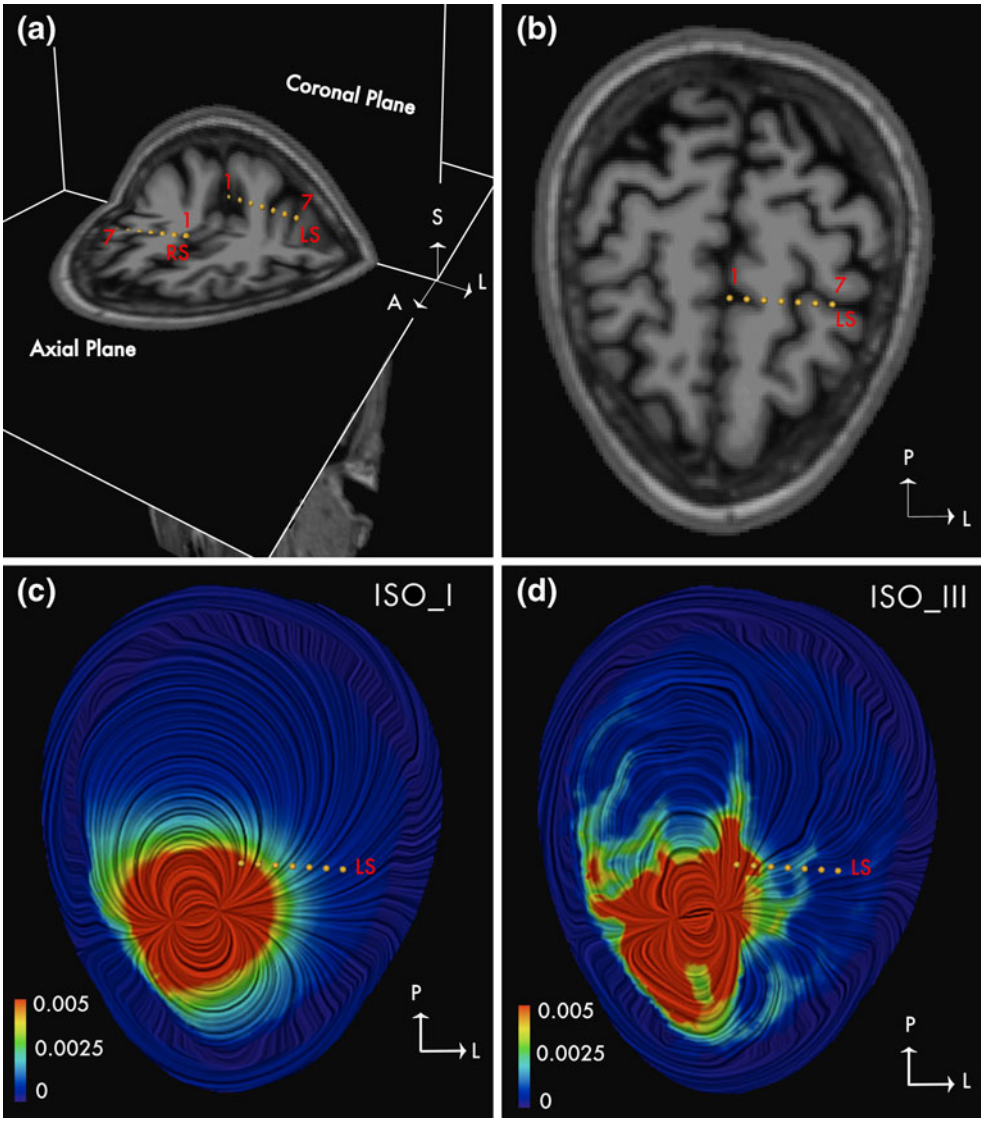

Fig. 4 *Influence of CSF on the volume currents.* The electric current density vector in an axial section is shown using LIC technique for a dipole at RS12 in subject BI18. The image is color coded with the magnitude of the current density vector and the direction is indicated by the texture. (**a**) Electrodes LS and RS are shown on coronal and axial T1-weighted MR images. Contact numbers 1 and 7 are marked. (**b**) Electrode LS shown on an axial T1-MRI scan; Contact numbers 1 and 7 are marked. (**c**) Current density in ISO_I: 3-tissue model shown in an axial plane containing electrode LS. (**d**) Current density in ISO_III: 15-tissue model shown in an axial plane containing electrode LS. Influence of CSF can be seen from the increased current density in regions containing CSF in ISO_III. Magnitude of the current density is in $\mu A/mm^2$

we look closely at stimulation sites where the anisotropic model ANISO_IC produced a smaller RDM than the isotropic model when compared to experimental data. Figure 5(a) shows that the fractional anisotropy is highest at contact 1 on electrode LC and is also closest to region of high anisotropy (corpus callosum) in subject BI18. High correspondence between experiment and model was obtained in BI18 for the dipole at LC12 where the RDM dropped from 15.5% for ISO_I and 20.2 % for ISO_III, to ~7% for ANISO_IC, with accurate fits at all electrode sites (<10% RDM). Similar improvements were also found at other stimulation sites in BI18 (such as RC23, RC45, RC67, RO23, RO45, RO56, LA12, LO12 and LO23) but the reduction in RDM when compared to isotropic case was one of the highest for site LC12. We now take the case of dipole at LC12 to study the differences in the current field between the isotropic and anisotropic models.

In Fig. 5(c, d and e) we plot the electric current density vectors using the LIC (linear integral convolution technique) due to a dipole at LC12 in isotropic models ISO_I, ISO_III and anisotropic model ANISO_IC, respectively. The direction of the volume currents can be seen from the texture using the LIC technique. Diffusion tensors, which define the anisotropic conductivity directions, are rendered as ellipsoids in Fig. 5(b). The figure shows a coronal plane containing the contacts LC1 and LC2. Regions of high anisotropy close to the stimulation site such as the corpus callosum and superior region of the corona radiata are marked in the figure. ISO_I clearly shows the classical dipolar pattern inside the intracranial volume. ISO_III now has a distortion in this pattern due to presence of CSF, ventricles and addition of gray matter (GM) and white matter (WM) as separate tissue types. At first glance, ANISO_IC looks very similar to the pattern generated by ISO_III; however a closer inspection shows the influence of

anisotropy in the medium. Current lines bend and bunch together to flow along the white matter fiber in the regions marked with the two arrows in Fig. 5(b) which represent the corpus callosum running in the mediolateral direction and the superior region of the corona radiata which runs in the superoinferior direction. To visualize the current lines closely, projections of the current density vectors in the vicinity of the two anisotropic regions are drawn on a coronal plane in Fig. 5(g and i). The diffusion tensor ellipsoids are shown in Fig. 5(f and h) to visualize the direction of the white matter fibers. Current vectors in isotropic model ISO_III are marked in red whereas the current vectors in ANISO_IC are marked in white. When compared to the direction of the isotropic current vectors (red arrows) in the corpus callosum for model ISO_III (Fig. 5(g)) addition of anisotropy in the model causes the anisotropic current vectors (white arrows) to deviate upwards in the mediolateral direction. Similarly in the superior region of the corona radiata, the anisotropic current vectors follow the direction of the fibers in the region and are deviated towards the center when compared to the isotropic current vectors in the same region (Fig. 5(i)).

To provide more support to the observations made above, in Fig. 6 we plot the cosine of the angle between the primary eigenvector of the white matter conductivity tensor and the electric current density vector (volume current vector) due to dipole at LC12 on a coronal section, which contained the stimulation electrode LC. The cosine (scaled between 0 and 1) is used as a similarity measure where 1 represents perfectly aligned vectors. In the isotropic case this alignment is by chance, but in the anisotropic case the cosine indicates close alignment between the current vector and white matter fibers. As seen from the figure, comparisons in the region bound by the rectangular box corresponding to the superior region of the radiata corona between the isotropic and anisotropic model shows that the alignment is largest for ANISO_IC and covers the whole region. The region in corpus callosum close to LC12 also shows increased alignment for ANISO_IC as compared to ISO_I and ISO_III (however the effect is less noticeable in the figure due to thresholding of the image between 0.7 and 1). This change of current direction in the superior region of the radiata corona explains the better fits at electrode site LS using the anisotropic model ANISO_IC for stimulation at site LC12 (since it lies between the 2 electrodes). Electrode RC was located on the opposite side of the corpus callosum from electrode LC with its first contact around 2-3 mm away from the corpus callosum in BI18. Figure 3(a) shows that ANISO_IC provided improved fits for measurements at electrode RC (3% RDM) when compared to ISO_I/ISO_III (10%/7% RDM) for stimulation at LC12. Similarly, for stimulation at RC12 the RDM at electrode LC reduced from 21% (for ISO_I) to 3% (for ANISO_IC). Figure 3(d) shows similar reductions in RDM at electrode LC for model ANISO_IC due to stimulations at RC23; thereby suggesting that the presence of anisotropy near the stimulation site has an influence on the forward solution. For subject BI15, and stimulation at contact RC12 (within few millimeters to corpus callosum with FA around 0.7), the anisotropic model ANISO_IC again provided with the largest reduction in RDM over all sensor locations (from 15% for both ISO_I and ISO_III to 8% for ANISO_IC; see Fig. 1C in supplementary section). Visualizations of current density vectors for stimulation site RC12 in BI15 (see Fig. 3 in supplementary section) yield observations similar to those made for site LC12 in subject BI18. Current lines follow white matter more closely in ANISO_IC (see current lines in corpus callosum marked in blue) than the isotropic models and thus deviate from the fields predicted by isotropic models.

We also observed decreases in RDM using ANISO_IC when the source was further away from regions of high FA for stimulation locations such as dipoles at RO23, RO45, RO56 and RO67 in BI18 (see Fig. 2(b)). RDM's show improved fits using ANISO_IC when compared to their isotropic counterparts. For example, there was a reduction in RDM from ~20% (ISO_III)/~21% (ISO_I) to ~9% (ANISO_IC) for dipole at RO23; reduction from ~27% (ISO_I)/~36% (ISO_I) to ~13% (ANISO_IC) for dipole at RO45; reduction from ~37% (ISO_I)/~37% (ISO_III) to ~13% (ANISO_IC) for dipole at RO56 and reduction from ~15% (ISO_I)/~16% (ISO_III) to ~9% (ANISO_IC) for dipole at RO56 (See Fig. 2(b)). Although these stimulation locations had a relatively low FA, these sites were embedded in the white matter. Electrode RO had contacts 2, 3 and 4 embedded in the white matter and is close to anterior region of the corona radiata. This suggests that white matter present in the pathway of the currents between the stimulation and recording site also influences the intracranial forward solution. For subject BI17, similar improvements were observed for sites on electrode LO with contacts 2 to 7 embedded in white matter with low FA. For site LO23, errors reduced from 32%/10% (ISO_III/ISO_I) to 6% (ANISO_IC) whereas for site LO45, errors reduced from 12%/9% (ISO_III/ISO_I) to 8% (ANISO_IC) (See Supplementary Fig. 1A). Similarly for subject BI15, we found reduction in errors at electrode RC from ~11% ISO_I and ISO_III to 3% (ANISO_IC) for stimulation site RO12 embedded in white matter (See Supplementary Figure 2C). Finally, for stimulation at site RC12 in BI15, the errors reduced from ~22%/~24% (ISO_III/ISO_I) to 10% (ANISO_IC) at electrode RO (See Supplementary Figure 2C). Both electrode RC and RO in BI15 had first 6 contacts in the white matter with contact 1 in electrode RC very close

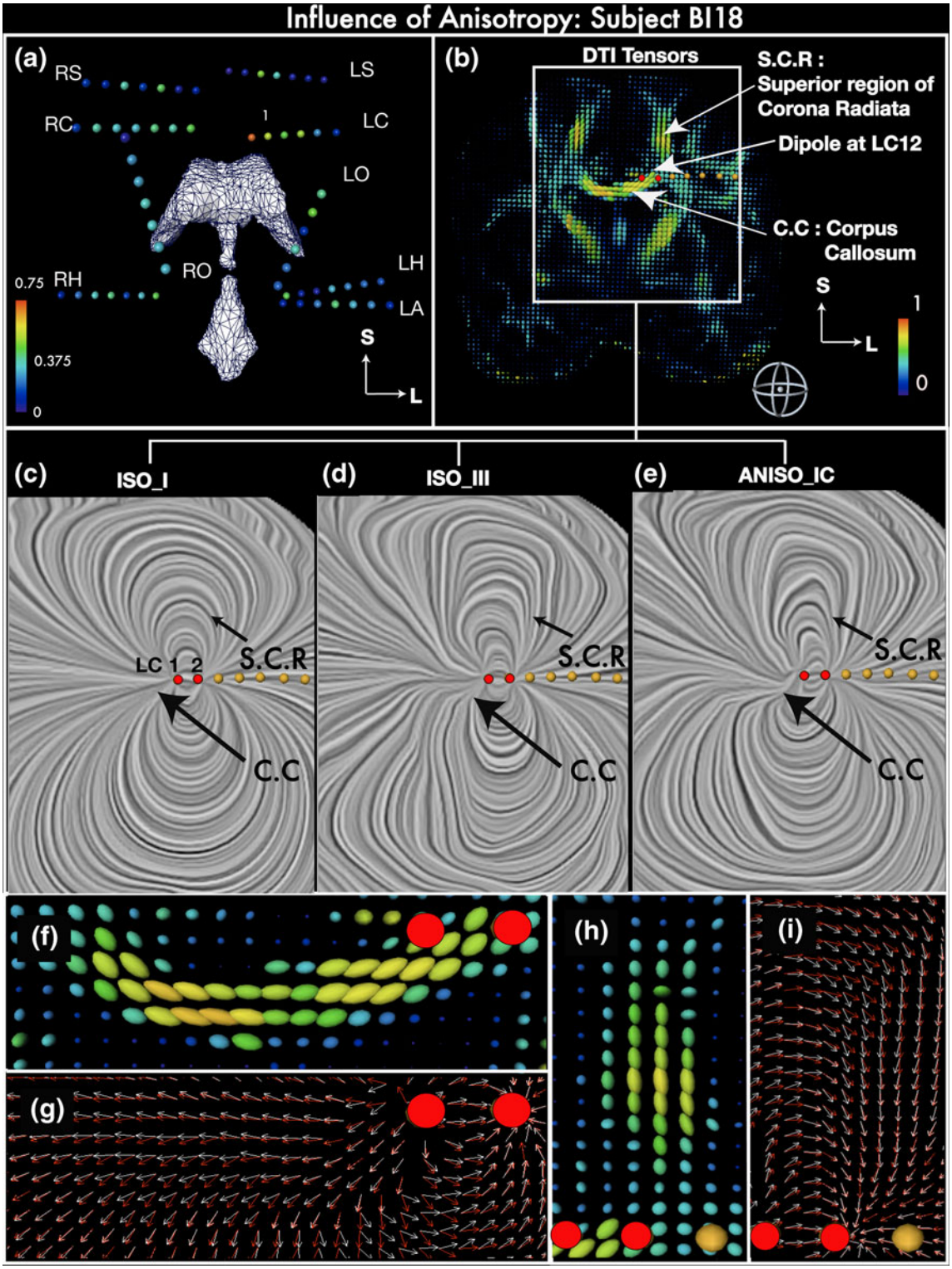
Influence of Anisotropy: Subject BI18
(a)
RS
LS
RC
1
LC
LO
RO
LH
RH
LA
0.75
0.375
0
S
L
(b)
DTI Tensors
S.C.R :
Superior region of
Corona Radiata
Dipole at LC12
C.C : Corpus
Callosum
S
L
1
0
(c)
ISO_I
(d)
ISO_III
(e)
ANISO_IC
LC 1 2
S.C.R
C.C
(f)
(g)
(h)
(i)

◀**Fig. 5** *Influence of anisotropy on the intracranial current flow.* (**a**) Coronal view of implanted depth electrode contacts in subject BI18 as spheres colored coded with the Fractional Anisotropy (FA) at the contact location. The spheres are rendered along with the ventricles (in white) to assist visualization of their approximate spatial locations. The deepest contact of the LA electrode is in or near the Left Amygdala, LH: Left Hippocampus, LS: Left Supplementary Motor, LC: Left Cingulate, LO: Left Orbito-frontal, RH: Right Hippocampus, RO: Right Orbito-frontal, RS: Right Supplementary Motor, RC: Right Cingulate. (**b**) DTI tensors in a coronal plane containing electrode LC in subject BI18, visualized as 3D ellipsoids color coded with FA values; the Corpus Callosum (C.C) and Superior region of corona radiata (S.C.R) are labeled. (**c**, **d, e**): Current density vectors in the region inside the white rectangular box in (B) are visualized using the LIC (Linear integral convolution) technique for a dipole at LC12 in model types ISO_I, ISO_III and ANISO_IC, respectively. The direction of the current is indicated by the texture. (**f, h**) 3-D renderings of diffusion tensor ellipsoids near stimulation site LC12 in C.C. and S.C.R., respectively. (**g, i**) Electric current density (ECD) vector near stimulation site LC12 in C.C. and S.C.R., respectively. White arrows indicate the current flow in the anisotropic white matter model ANISO_IC whereas red arrows indicate the direction of the current in the isotropic model ISO_III. Red dots in panels B-I indicate contacts LC1 and LC2. Another example is shown in Supplementary Figure 3 (dipole RC12 in subject BI15)

(within 2 mm) to corpus callosum. Thus, there was a systematic improvement in accuracy from using anisotropy in the model, especially when the stimulating dipole or recording contacts, or intervening tissue, exhibited high anisotropy.

3.4 Comparison between anisotropic models

Assigning a constant value to the anisotropy produced models (ANISO_WM_II_abcd) with generally poor performance. Anisotropic model ANISO_WM_II_d had the worst performance of all the anisotropic models in all subjects as seen in graph plotted in Fig. 2. Conversely, the anisotropic models assuming a linear relation between diffusivity and conductance (ANISO_WM_I and ANISO_IC) had excellent performance, clearly out-performing the models with constant anisotropy. Some evidence was found in subject BI18 for more accurate modeling when including anisotropic information for gray matter and sub-cortical elements from DTI in ANISO_IC. Electrode LH had its four contacts embedded in tissue labeled as ‘sub-cortical’ while electrode LA had first 2 contacts embedded in tissue labeled as ‘sub-cortical’. This ‘sub-cortical tissue’ is assumed isotropic in model ANISO_WM_I whereas ANISO_IC incorporates the linear anisotropic model for the sub-cortical elements using

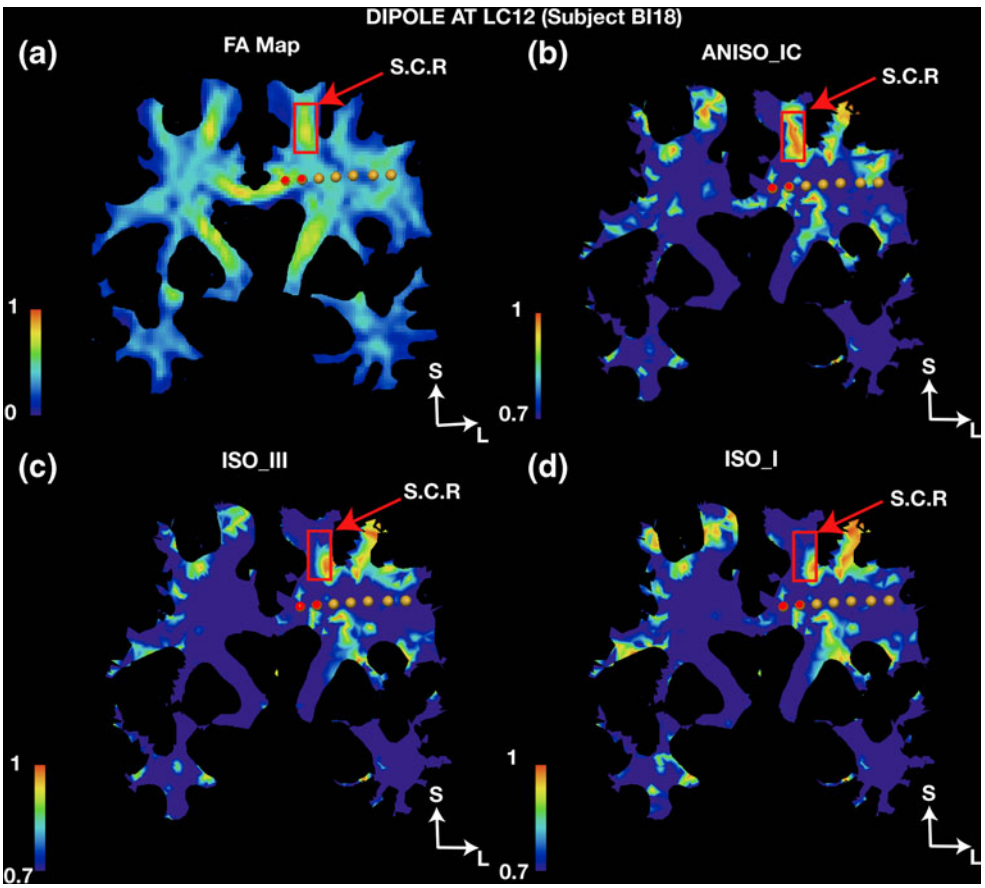

Fig. 6 *Alignment of current flow with white matter fiber direction under different models*. (**a**) Coronal section containing electrode LC shows fractional anisotropy (FA) in the white matter. Superior region of corona radiata is marked by the rectangular box and labeled as ‘S.C.R’. (**b**) Alignment of the current vectors with the white matter fibers is visualized by calculating the cosine of the angle between the primary eigenvector of the conductivity tensor and the electric current density vector calculated due to dipole at LC12 in the anisotropic model, ANISO_IC. (**c**) Same, using the 15 tissue isotropic model, ISO_III. (**d**) Same, using the 3 tissue model, ISO_I. Cosine values closer to 1 indicate a higher degree of alignment

DTI information (identical to the proportional constant used for white matter in ANISO_WM_I). We found reductions in the overall RDM for stimulation at LA12 from 20% (using ANISO_WM_I) to 9% (using ANISO_IC) as seen in Fig. 2(b). A closer inspection of the RDM's at each electrode in Fig. 3(c) shows that for stimulation at LA12 inclusion of anisotropy in the sub-cortical elements causes reduction of errors at LH from ~21% to ~8%. There was a marked reduction in errors due to stimulations at LO12 using ANISO_IC when compared to ANISO_WM_I, which was due to improved fits at electrode LA and LH (see Fig. 3(b)). Thus, modeling of intracranial electric field is more accurate when the level of anisotropy is estimated in each voxel using information from DTI.

4 Discussion and conclusions

In this paper, we presented the validation of a realistic anisotropic model for brain tissue using electric potentials generated by stimulation of an implanted artificial dipole in human subjects. We examined differences in the electric current flow within the head between a variety of models, varying in the compartments they contained, whether they included anisotropy, and if so, how the anisotropic conductivity was estimated. A combination of CT, T1-MRI, PD-MRI and DTI was used to generate the head models. Quantitative measures like RDM and novel visualization tools are used to complement and understand the differences between the models in a more comprehensive manner. Previous studies have provided meaningful insights to the influence of anisotropy on EEG fields using simulations (Haueisen et al. 2002) as well as advanced visualization techniques (Wolters et al. 2006) but have lacked experimental data to support their conclusions. To our knowledge, the study presented in this paper is first of its kind to investigate in a detailed fashion the electric fields generated intracranially due to a current dipole in a human subject using a realistic FEM model which includes brain anisotropy. The measurements at the depth electrodes represent a sparse sampling of the field. However our previous simulation study (Bangera et al., manuscript in submission) using a large number of randomly selected locations as well as the limited experimental sensor locations in subject BI18 suggested that it was feasible to make reliable observations using the experimental electrode locations. The simulation study, which also involved comparisons between different forward models showed large differences in the electric fields. These changes were caused as a result of adding more detail in the model particularly the CSF and anisotropy. Experimental data helps us clarify which of the models predict fields that match reality. By observing the tissue environment around specific dipole locations and measurement locations affect the correspondence between model predicted values and experimental data, we can infer the characteristics needed for an accurate forward model.

4.1 Linear anisotropic model more accurate than global anisotropic model

An anisotropy ratio of 10:1 between the conductivity along the white matter fiber directions, versus perpendicular to that direction, has been reported in literature (Nicholson 1965). This ratio has been used for conducting simulation studies of the effects of anisotropic white matter in the brain on EEG topography (Wolters et al. 2006). The model ANISO_WM_II_d that utilized this anisotropic ratio had the worst performance of all the anisotropic models in our study. This is not a surprising result, since the 10:1 ratio can be considered as an upper bound on the anisotropy ratio for white matter fibers. The failure of ANISO_WM_II to provide good fits confirms that the assumption of a global anisotropic ratio of 10:1 for white matter in EEG/MEG forward models is erroneous. In contrast, the anisotropic model ANISO_IC provided the best fit of all the models. This provides an experimental validation for the assumption that the conductivity tensor and diffusion tensor share eigenvectors. Further, the success of a model that assumes a linear relationship between their eigenvalues ($\sigma_\lambda/d_\lambda \approx 0.5708$) supports the method of quantitatively inferring the conductivity anisotropy from non-invasive DTI measurements of the water self-diffusion process in the human brain as proposed by Tuch et al. (Tuch et al. 2001). isualizations in Fig. 5 clearly show that anisotropy in white matter influences the return currents when the activated dipole is close to a region of high anisotropy. Return currents are not aligned completely with fiber directions but are rather diverted in the general direction of the fibers with more alignment than the isotropic case. Thus changes in potential topography generated by ANISO_IC when compared to ISO_III are not as drastic as the one that would occur in models where a strong anisotropic ratio is assumed (such as in ANISO_WM_II). Error reductions were also observed at measurement locations embedded in white matter with low FA. Additional specific improvements were found when anisotropy was modeled in gray matter including subcortical structures as well as white matter (i.e., in the model ANISO_IC in comparison to ANISO_WM_I). These results agree with the observations made in previous simulation studies (Haueisen et al. 2002; Wolters et al. 2006) which found appreciable changes in intracranial potential topography inside the brain for deep sources embedded in the white matter. The two studies however used two different models for anisotropy; the study by Haueisen et al. (2002) utilized the linear anisotropic model whereas the study by Wolters et al. utilized the global anisotropic model.

4.2 Role of CSF

Along with anisotropy, inhomogeneity also plays an important role in defining the EEG topography. CSF provides regions of higher current density, which was visualized in Fig. 4. These agree with the observations made using similar visualizations by Wolters et al. (2006). By using a measurement electrode with multiple contacts in CSF (LS) and a stimulation dipole location closer to CSF (RS12, which is close to the inter-hemispheric space filled with CSF), the improvements in RDM using ISO_III over model ISO_I show that the CSF layer is crucial for accurate predictions of intracranial potentials in these regions. Inspite of the improvements in predicted values due to the inclusion of CSF in isotropic models ISO_II and ISO_III, experimental comparisons show that on the whole, average errors in isotropic model without CSF (ISO_I) are smaller than the errors using isotropic model with CSF (ISO_II and ISO_III). We speculate that the removal of CSF compensates for the lack of anisotropy in ISO_III and results in an "average" potential topography that is closer to the actual topography and provides improved performance of ISO_I (compared to ISO_III) at certain locations.

4.3 Limitations

Accurate representation of the electrical properties of cortical tissue in forward models for extracellular fields is still a challenge due to its dependence on measurement frequency and variability in values reported in literature. Recent studies (Bédard et al. 2004; Butson et al. 2006) have suggested that inclusion of reactive elements in a forward model with inhomogeneous media might be necessary to mimic the frequency dependence of extracellular media and explain the frequency-dependent attenuation of extracellular potentials in cortex. Due to a lack of provision to include reactive elements in the FEM software used in our analysis and also to keep the computational burden at a manageable level, our model was limited to include purely resistive elements. Thus, the representation of electrical properties of tissues in the model can be improved upon and this will be investigated in a future study. The resolution of the linear anisotropic model used in this study was limited by the resolution of the diffusion tensor images (2 x 2 x 2 mm voxel) and the resolution of the FEM element size (average edge length of 2.5 mm). A further reduction in the errors can be expected by obtaining DTI information at 1 mm^3 voxel size and generating smaller FEM elements (with an average edge length of 1 mm). The linear scaling used between the eigenvalues of the conductivity and water self-diffusion tensors is assumed to be a constant for each FEM tetrahedral element used in the model. This is still an approximation, since a variation in the scaling factor for each element can be expected based on variations in the volume of each element in the model. Although the meshing algorithm generates mesh elements of approximately the same size, there is a small amount of variability in the element size, which is not taken into account. There was inter-subject variability in our results with the major findings obtained from subject BI18. As mentioned before, this discrepancy is attributed to the improved experimental protocol used for subject BI18 as compared to the other three subjects, which led to a wider coverage of stimulation and measurement sites in BI18. In general, experimental evidence at several locations in the three subjects did support the importance of including anisotropy for accurate models; however we expect that the impact of anisotropy on the average errors would have been larger if all subject had a complete data set. The only previous intracranial study by Smith et al. (Smith et al. 1983) based on measurements over a single electrode claimed that a homogeneous model can be used for accurate calculation of fields at distances greater than 2 cm from the source. Our results clearly do not support that claim since effects of anisotropy and inhomogeneity were observed for distances over 2 cm from the source. The study by Smith et al. (1983) however clearly demonstrates the pitfalls of using a sparse recording montage in testing the nature of electric fields in an inhomogeneous and anisotropic medium such as the brain. Considered as a whole, the results from our study support the hypothesis that a detailed description of intracranial tissue including inhomogeneity and anisotropy is necessary to generate accurate intracranial forward solutions. Incomplete models could possibly lead to higher errors when certain details (such as anisotropy) in the model (ISO_III) are ignored. With the aid of advanced visualization tools and experimental data, we substantiate the need for further studies using realistic head models for improved source reconstructions in the field of bioelectric source imaging.

Acknowledgements The authors would like to first and foremost acknowledge the selfless co-operation of the patients who participated in this study. The authors would like to thank Lawrence Gruber, Frank Kampmann and the EEG technicians from the EEG laboratory at the Beth Israel Deaconess Medical Center for their assistance in set-up and collection of the data. In addition, the authors would like to thank the Scientific Computing and Visualization Center (http://scv.bu.edu) at Boston University for proving access to the FEM software used in our analysis. This study was financially supported by NIH grants NS44623/NS18741 and Trustees of Boston University.

Appendix A

Biphasic pulse generation

The biphasic square pulse was generated via software, which provided control on the flat portions of the square wave with rounding of edges of the square waves (to avoid stimulus artifacts). A simple rectangular pulse passed through an EEG amplifier would produce a recorded waveform with decreasing amplitude during the pulse. The 'droop' of the square pulse refers to this change in slope of flat portions of the square pulse due to the high pass filtering effects of the amplifiers. The software provides a compensating 'upslope', which counteracts the droop imparted by the amplifiers and helps in generating square pulses with flat portions during voltage measurements. With this waveform (see Fig. 1(d)), it is possible to average the amplitude across the constant portions of the recorded pulse thereby improving the signal-to-noise ratio of the recorded signals.

Signal to Noise Ratio (SNR) calculation

SNR of the signal is calculated using the same method as that used by Cuffin et al. (Cuffin et al. 2001). For the square pulse shown in Fig. 1(e), samples are averaged over the positive and negative phase of the pulse. The signal is taken as the difference of the averages sampled over the positive and negative phases of the pulse. For a sampling rate of 2000 Hz and pulse duration/per phase of 15 ms, this corresponds to an average of 30 samples over each phase. The noise is defined as the RMS values of 30 samples in the pre-pulse interval. The SNR is calculated as the average of the SNR calculated as above for all channels.

Appendix B

Optimized conductivity was obtained by minimizing the forward solution cost function (error variance between model predicted value and experimentally measured electric potential values). The average conductivity value for each intracranial tissue in the frequency range of interest for bioelectric activity (<1 kHz) was obtained from literature and used as the seed point for optimization. The damped Newton's method was employed for the optimization routine. The optimization problem is formulated as below:

$$\sigma* = \arg\min_{\sigma} f(\sigma) \quad \text{where } f : R'' \mapsto R \tag{B.1}$$

$$f(\sigma_1, \sigma_2, \ldots, \sigma_n) = GF^2 \text{ where } GF(V_{calc}, V_{meas}) = \frac{\sqrt{\sum_{i=1}^{m} \left(V_{calc}^i - V_{meas}^i\right)^2}}{\sqrt{\sum_{i=1}^{m} \left(V_{meas}^i\right)^2}} \tag{B.2}$$

References

Akhtari, M., Bryant, H. C., Mamelak, A. N., Flynn, E. R., Heller, L., Shih, J. J., et al. (2002). Conductivities of three layer live human skull. *Brain Topography, 13*(3), 151–167.

Basser, P. J., Mattiello, J., & LeBihan, D. (1994). MR diffusion tensor spectroscopy and imaging. *Biophysical Journal, 66*, 259–267.

Baumann, S. B., Wozny, D. R., Kelly, S. K., & Meno, F. M. (1997). The electrical conductivity of human cerebrospinal fluid at body temperature. *IEEE. Trans. Biomed. Eng., 44*(3), 220–223.

Bédard, C., Kröger, H., & Destexhe, A. (2004). Modeling Extracellular Field Potentials and the Frequency-Filtering Properties of Extracellular Space. *Biophysical Journal, 86*(3), 1829–1842.

Burger, H. C., & Van Milaan, J. B. (1943). Measurement of the specific resistance of the human body to direct current. *Acta. Med. Scand., 114*, 584–607.

Butson, C. R., Cooper, S. E., Henderson, J. M., & McIntyre, C. C. (2006). Patient-specific analysis of the volume of tissue activated during deep brain stimulation. *Neuroimage, 34*(2), 661–670.

Cohen, D., Cuffin, B. N., Yunokuchi, K., Maiewski, R., Purcell, C., Cosgrove, G. R., et al. (1990). MEG versus EEG Localization Test Using Implanted Sources in the Human Brain. *Ann. Neurol., 28*, 811–817.

Cuffin, B. N. (1998). EEG dipole source localization. IEEE Engineering in Medicine and Biology: 118-122.

Cuffin, B. N., Cohen, D., Yunokuchi, K., Maiewski, R., Purcell, C., Cosgrove, G. R., et al. (1991). Tests of EEG Localization Accuracy Using Implanted Sources in the Human Brain. *Ann. Neurol., 29*, 132–138.

Cuffin, B. N., Schomer, D. L., Ives, J. R., & Blume, H. (2001). Experimental tests of EEG source localization accuracy in spherical head models. *Clinical Neurophysiology, 112*(1), 46–51.

Gabriel, S., Lau, R. W., & Gabriel, C. (1996). The dielectric properties of biological tissues: III. *Parametric models for the dielectric spectrum of tissues. Phys. Med. Biol., 41*, 2271–2293.

Geddes, L. A., & Baker, L. E. (1967). The specific resistance of biological materials: A compendium of data for the biomedical engineer and physiologist. *Med. Biol. Eng., 5*(3), 271–293.

Haueisen, J., Tuch, D. S., Ramon, C., Schimpf, P. H., Wedeen, V. J., George, J. S., et al. (2002). The Influence of Brain Tissue Anisotropy on Human EEG and MEG. *NeuroImage, 15*, 159–166.

Henderson, C. J., Butler, S. R., & Glass, A. (1975). The localization of equivalent dipoles of EEG sources by the application of electrical field theory. *Electroenceph. Clin. Neurophysiol., 39*, 117–130.

Latikka, J., Kuurne, T., & Eskola, H. (2001). Conductivity of living intracranial tissues. *Phys. Med. Biol., 46*, 1611–1616.

Law, S. K. (1993). Thickness and resistivity variations over the upper surface of the human skull. *Brain Topography, 6*(2), 99–109.

Leahy, R., Mosher, J. C., Spencer, M. E., Huang, M. X., & Lewine, J. D. (1998). A study of dipole localization accuracy for MEG and EEG using a human skull phantom. *Electroenceph. Clin. Neurophysiol., 107*(2), 159–173.

Lindenblatt, G., & Silny, J. (2001). A model of the electrical volume conductor in the region of the eye in the ELF range. *Phys. Med. Biol., 46*, 3051–3059.

Malte Zöckler, D. S., Hans-Christian Hege (1996). Interactive visualization of 3D-vector fields using illuminated stream lines. Proceedings of the 7th Conference on Visualization,IEEE Visualization 107-113.

Mccreery, D. B., Agnew, W. F., Yuen, T. G. H., & Bullara, L. (1990). Charge Density and Charge Per Phase as Cofactors in Neural Injury Induced by Electrical Stimulation. *IEEE. Trans. Biomed. Eng., 37*(10), 996–1001.

Meijs, J. W. H., Weier, O., Peters, M. J., & Van Oosterom, A. (1989). On the numerical accuracy of the boundary element method. *IEEE. Trans. Biomed. Eng., 36*, 1038–1049.

Merill, D. R., Bikson, M., & Jeffreys, J. G. R. (2005). Electrical stimulation of excitable tissue: design of efficacious and safe protocols. *Journal of Neuroscience Methods, 141*, 171–198.

Nicholson, P. W. (1965). Specific impedance of cerebral white matter. Exp. Neurol.(13): 386-401.

Okada, Y. C., Huang, J.-C., Rice, M. E., Tranchina, D., & Nicholson, C. (1994). Origin of the apparent tissue conductivity in the molecular and granular layers of the *in vitro* turtle cerebellum and the interpretation of Current Source-Density analysis. *J. Neurophysiol., 72*, 742–753.

Oostendorp, T. F., Delbeke, J., & Stegeman, D. F. (2000). The Conductivity of the Human Skull: Results of *In Vivo* and *In Vitro* Measurements. *IEEE. Trans. Biomed. Eng., 47*(11), 1487–1492.

Plummer, C., Litewka, L., Farish, S., Harvey, A. S., & Cook, M. J. (2007). Clinical utility of current-generation dipole modelling of scalp EEG. *Clinical Neurophysiology.* doi:10.1016/j.clinph.2007.08.016.

Ranck, J. B., & Be Meritt, S. L. (1965). The specific impedance of the dorsal columns of cat; an anisotropic medium. *Exp. Neurol., 11*, 451–463.

Salu, Y., Cohen, L. G., Rose, D., Sato, S., Kufta, C., & Hallett, M. (1990). An improved method for localizing electric brain dipoles. *IEEE. Trans. Biomed. Eng., 37*(7), 699–704.

Smith, D. B., Sidman, R. D., Henke, J. S., Flanigin, H., Labiner, D., & Evans, C. N. (1983). Scalp and Depth recordings of induced deep cerebral potentials. *Electroenceph. Clin. Neurophysiol., 55*, 145–150.

Smith, D. B., Sidman, R. D., Flanigin, H., Henke, J., & Labiner, D. A. (1985). Reliable method for localising deep intracranial sources in the EEG. *Neurology, 35*, 1702–1707.

Tehovnik, E. J. (1996). Electrical stimulation of neural tissue to evoke behavioral responses. *Journal of Neuroscience Methods, 65*, 1–17.

Tuch, D. S., Wedeen, V. J., Dale, A. M., George, J. S., & Belliveau, J. W. (2001). Conductivity tensor mapping of the human brain using diffusion tensor MRI. *PNAS, 98*(20), 11697–11701.

Ulbert, I., Halgren, E., Heit, G., & Karmos, G. (2001). Multiple multielectrode recording system for human intracortical applications. *J. NeuroScience Methods, 106*, 69–79.

Visage Imaging, Inc. (2007). AMIRA - Advanced 3D Visualization and Volume Modeling. Carlsbad, CA.

Wolters, C. H. (2003). Influence of Tissue Conductivity Inhomogeneity and Anisotropy on EEG/MEG based Source Localization in the Human Brain, PhD Thesis. Mathematics, University of Leipzig. PhD**:** 253.

Wolters, C. H., Anwander, A., Tricoche, X., Weinstein, D., Koch, M. A., & MacLeod, R. S. (2006). Influence of tissue conductivity anisotropy on EEG/MEG field and return current computation in a realistic head model: A simulation and visualization study using high-resolution finite element modeling. *Neuroimage, 30*(3), 813–826.